

# Cold-Workability Limits for Carbon and Alloy Steels

A. El-Domiaty

(Submitted 6 January 1998; in revised form 3 December 1998)

In metalforming, the success in accomplishing the required deformation without failure of the forming tools or cracking of the work material represents the major concern for manufacture and design engineers. The degree of deformation that can be achieved in a particular metalworking process without creating an undesirable condition is defined as workability. In the present work, an experimental investigation was carried out to determine the cold-workability limits for five different types of steel: AISI 1018, 1045, 1078, 4140, and 4340. The upset (compression) test was used to determine the workability limit for each type. The upset dies and specimen geometries were designed to give different strain paths covering the range from homogeneous deformation ( $\epsilon_z/\epsilon_\theta = -2.0$ ) to close to plane-strain condition ( $\epsilon_z/\epsilon_\theta = 0.0$ ). Grid pattern was printed on the specimen surface in order to measure the axial and hoop strain components during deformation. Specific elements were selected on the specimen surface, and their strain paths were determined. Each strain path was terminated once surface cracking had been observed. The ends of the strain paths, at which macrocracks were observed, were connected to obtain the workability limit on the forming-limit diagram. The workability limit of AISI 1018 is the highest among the other types of steel.

**Keywords** bulk forming, ductile fracture, forgability, metalworking, upsetting, workability

## 1. Introduction

The term workability is usually defined as the relative ease with which a metal or alloy can be shaped through plastic deformation. The evaluation of workability involves both measurement of the resistance to deformation (strength) and the amount of plastic deformation before fracture (ductility). Therefore, a complete description of the workability of a material is specified by its flow-stress dependence on processing variables (strain rate, die temperature, preheat temperature, etc.), its failure behavior, and the metallurgical factors that control the microstructure of the material. The limits of workability can be considered cracking or ductile fracture, but there may be other conditions such as poor surface finish, buckling, formation of loops in forging, and unsatisfactory mechanical properties such as poor fracture toughness or fatigue strength.

A large number of tests are currently used to evaluate the workability of a material. A brief introduction of these tests is given by Dieter (Ref 1). The primary tests are tension, torsion, compression, and bending. The compression test has been the most highly developed as a workability test. In this test, a cylindrical specimen is upset between two dies. The average stress state during testing is similar to that in many bulk deformation processes. Therefore, a large amount of deformation can be achieved before fracture occurs. The stress state can be varied over wide limits to obtain different strain paths by controlling the barreling of the specimen through variation in geometry and by reducing friction between the specimen ends and the forming dies. Unless the lubrication condition at the specimen/forming-tool interface is very good, frictional restraint

will retard the outward motion of the end face and part of it will be formed by the sides of the original cylinder folding over. Moreover, the barreling that results introduces a complex stress state, which is beneficial in fracture testing, but detrimental when the test is used to determine the flow stress.

The main factors affecting workability limits are material factors and process factors. The material factors include fracture mechanics, flow localization, and metallurgical considerations. The process factors include strain and strain distribution, strain rate and temperature, friction, and stress state in working.

### Nomenclature

$d\epsilon_r$	Infinitesimal strain component in the radial direction
$d\epsilon_z$	Infinitesimal strain component in the axial direction
$d\epsilon_\theta$	Infinitesimal strain component in the hoop direction
$h_i$	Current height
$h_o$	Initial height
$H_o/D_o$	Aspect ratio
$K$	Strength coefficient
$n$	Strain-hardening exponent
$w_i$	Current width
$w_o$	Original width
$\alpha$	Stress ratio
$\beta$	Strain ratio (slope of the strain path)
$\epsilon_z$	Axial strain
$\epsilon_\theta$	Hoop strain
$\bar{\epsilon}$	Effective strain
$\bar{\sigma}$	Effective stress
$\sigma_m$	Mean stress component $[(\sigma_r + \sigma_\theta + \sigma_z)/3]$
$\sigma_r$	Radial stress component
$\sigma_z$	Axial stress component
$\sigma_\theta$	Hoop stress component

A. El-Domiaty, Suez Canal University, Faculty of Engineering, Port Saied, Port-Fouad, Egypt, 42523.

More details about these factors are given in Ref 2. The effects of these factors on the workability limits have been studied extensively over the last 20 years. A brief review of the previous work is given in the next section.

Kudo and Aoi (Ref 3) used the apparent disadvantage of barreling to obtain different strain paths. Concentrically grooved dies lead to severe barreling and early fracture (steep strain path), while well-lubricated dies result in less barreling and later fracture (long strain path). For very good lubrication, the strain path should approach homogeneous compression condition. Two types of cracks were observed. Vertical cracks occur in specimens subjected to severe end constraint, and oblique cracks occur in specimens tested with well-lubricated dies. The effect of end conditions as well as the height-to-diameter ratio for a cylindrical specimen on the workability limits have also been studied by Kudo et al. (Ref 4). The authors of Ref 4 suggested also that the hydrostatic component of stress state has a considerable effect on the workability limit. Based on the experimental measurements obtained from upset tests for a solid cylindrical specimen, Kobayashi (Ref 5) developed a tentative analysis for the relationship between barreling and strains at the free surface.

Hoffmanner (Ref 6) carried out an experimental program to determine the workability limits from the accurate determination of the actual stress state under which aluminum alloy 2024-T351 and AISI 1095 are deformed. Two fracture modes were detected confirming Kudo and Aoi's results (Ref 3). The effect of end restraint on barreling of the free surface and on the strain path was investigated by Shah (Ref 7). For lubricated ends held in die depressions, fracture was found to be parallel to the specimen axis. For lubricated ends with flat die, cracks were found at approximately  $45^\circ$  to the specimen axis. Levy and Fine (Ref 8) carried out an experimental work to determine the workability limits in upsetting of AISI 1008, 1018, 1024, and 1045 steel specimens having an aspect ratio ( $H_o/D_o$ ) in the range of 0.31 to 2.41, under different deformation ratios. Compositional variations among different types of steel were found to have no effect on the surface strain distribution or on barreling in upsetting. It was also found that the folding over of the side surface and barreling in general become more pronounced as the reduction percent increases and  $H_o/D_o$  decreases, and also the lubricant effectiveness decreases.

Pure aluminum was used by Thomason (Ref 9, 10) to analyze the history of plastic flow of steels. Thomason used the plastic-strain increment equations and Hill's yield criterion to determine the tensile stress component generated on the free surface. This component is governed by friction and specimen geometry and promotes fracture at the equator. Thomason (Ref 9) tried also to estimate the exact location at which tensile plastic instability occurs at the equatorial free surface of the specimen.

Kuhn and Lee (Ref 11) developed a refined method for measuring the localized surface strains in upsetting of cylindrical specimens. The method was carried out on AISI 1045 steel using various end conditions. The workability limits for AISI 1020, 1045, and 303 stainless steel were determined by Lee and Kuhn (Ref 12) using upset tests for cylindrical specimens having  $H_o/D_o$  in the range 0.75 to 1.5 and under different friction conditions. Observation of cracks by the naked eye on the free

surface was considered the limit of deformation. The possibility of predicting the onset of fracture in bulk deformation processes was studied by Woodall and Schey (Ref 13). They tried to correlate the limit strains obtained from simple tests with those measured in upsetting with sticking frictional condition at the specimen/die interface and in the rolling process. In rolling, strain paths were straight. However, in upsetting, barreling occurred and caused a gradual shift of the strain path from linearity. Woodall and Schey (Ref 13) showed also that the strains at fracture in upsetting and rolling fall on a line of  $-0.5$  slope in the forming-limit diagram (FLD). Oh and Kobayashi (Ref 14) investigated the workability of aluminum alloy 7075-T6 in upsetting and rolling at room temperature, considering cracking on the free surface to be the limit of deformation. Fracture strains were shown to lie on a  $(-0.5)$  slope line.

Bariani (Ref 15) discussed the effect of high strain rate and heat generation during upsetting for 1100, 2024, and 7075 aluminum alloys. It was found that in spite of the drastic temperature increase, the cold workability of the three materials was not affected, neither in critical reduction in height values, nor in typical straight-line fracture loci. A theoretical method was developed by Bariani (Ref 15) to calculate the stress ratio, depending on an admissible velocity field suggested by Kobayashi (Ref 5), and the specimen geometry at every step of the deformation process.

Both upsetting and bolt-heading processes for 303 stainless steel gave similar experimental strain paths as obtained by Shah and Kuhn (Ref 16). A statistical procedure was adopted in their analysis in order to obtain formulas that could be used to predict the percentage height reduction and the percentage diameter increase. Erman et al. (Ref 17) used flanged and tapered specimens in addition to cylindrical specimens to get strain paths close to the plane strain condition (i.e., no straining in the axial direction). Their work was performed on 2024-T351 aluminum, AISI 1045, and AISI 4640 sintered steel powder. Both 2024 T351 aluminum and AISI 4640 sintered steel powder gave straight-line fracture phenomenon, while AISI 1045 gave a dual-slope fracture line. The same phenomenon was observed for 2024-T4 aluminum alloy at  $300^\circ\text{C}$  and strain rate of  $0.1\text{ s}^{-1}$  during the upset process. Kiviruori and Sulonen (Ref 18) carried out experimental work to determine the surface stresses and the strain paths of cylindrical steel specimens in upsetting. The results obtained suggested the addition of another line to the fracture locus. A third fracture mode, called double oblique crack, was also introduced. The simultaneous existence of maximum value of hoop and axial stress is the main reason for initiation of double oblique cracks. Sornberger et al. (Ref 19) used the cold upset testing method to assess the ductility of continuous-cast 5065 aluminum alloy. The fracture limits were obtained, and three zones were identified, each corresponding to certain criterion of fracture, except the third zone.

The effect of the presence of longitudinal surface defects on fracture during upsetting had been investigated by Thomason (Ref 20). He found severe reduction in the ductility of grooved specimens. The apparent ductility of grooved specimens was found to increase as the  $H_o/D_o$  increased. Mayagawa et al. (Ref 21) showed that cracking always initiates at the root of the notch when V-type notches are machined on the surface of the specimens. Specimens having closed artificial notches on their

surfaces were upset by Fukuda and Hajita (Ref 22). They tried to correlate the carbon content and depth of notch to the upsetting limit.

The predeformation effect on the workability of steel cylindrical specimens was studied by Kojima and Tozawa (Ref 23). They found that the upsetting limits for predrawn specimens with and without longitudinal grooves generally increase as the amount of predeformation increases up to about 20% for steel having 0.45% C. Any increase of more than 20% predeformation gave lower upsetting limits.

The grain size effect on ductile fracture of polycrystalline metals and alloys has been studied. The recent study by Fan (Ref 24) indicated that the effect of grain boundaries on the fracture toughness is complex; they can either toughen and enhance the grain-boundary deformation or cause embrittlement by promoting microvoid nucleation in the grain-boundary zone. The porosity of the material also has a great effect on the workability of the material. The work by El-Domiati and Shaker (Ref 25) on porous-steel preforms showed that the increase in porosity percentage caused a higher reduction in workability limit.

In recent years, researchers have tried to implement ductile fracture criteria in available finite-element programs for metal-forming analysis. Clift et al. (Ref 26) utilized an elastic-plastic finite-element formulation to solve formability problems of simple upsetting, extrusion, and strip compression and tension. Zhu et al. (Ref 27) presented a theoretical study based on another elastic-plastic finite-element formulation to investigate the potential of several published workability criteria in predicting fracture-initiation sites during plane-strain side pressing of cylinders. Wifi et al. (Ref 28) proposed a general benchmark test for comparing different fracture criteria and concluded that there is a need for performing more numerical and experimental support work to validate the various fracture criteria. The assessment of various empirical and semiempirical ductile fracture criteria to determine their ability to predict the occurrence of ductile fracture in metalforming processes was carried out recently by Shabara et al. (Ref 29). The limit strains or the forming limit corresponding to six ductile fracture criteria were determined and compared with experimental data. Fracture strains using cylindrical, ring, tapered, and flange specimens were determined by Gouveia et al. (Ref 30) to investigate the validity of the workability criteria under conditions of stresses and strains similar to those usually found in bulk metal-forming processes. They found only two criteria that successfully predict the locations of ductile fracture.

In order to simplify the problem of representing workability, an assumption is made by introducing a straight-line relationship between the workability function (strain to fracture) and stress-formability index,  $\beta$ , proposed by Vujovic and Shabaik

(Ref 31). The stress-formability index ( $\beta = 3\sigma_m/\sigma_{eff}$ ) represents the effect of both the hydrostatic and the effective stress components. Wagener and coworkers (Ref 32, 33) argued that the increase of the hydrostatic pressure in the forming zone by the application of a counterforce gave an increase of the workability. They also adopted the idea of straight-line relationship between the strain to fracture and the workability index ( $\beta$ ). To eliminate the problem of higher slope in this straight-line relationship, the line is assumed to pass through the strain values corresponding to both obtained from simple tension and compression tests. This assumption was adopted also by Abdel-Rahman (Ref 34) who gave an equation of the straight-line relationship between the fracture strain and the workability index. The slope of that line was given as  $-(\epsilon_{comp} - \epsilon_{ten})/2$ .

Because the use of any available workability or ductile fracture criterion requires at least the value of the fracture strain at two points on the fracture locus, the object of the present work is to determine experimentally a complete fracture locus for five steel grades. These types of steel were chosen for their industrial importance. AISI 1018 steel is a plain-carbon steel of medium-to-low carbon content and is widely used in cold forming. It is used typically for machine bases and machine parts. AISI 1045 is a plain-carbon steel of medium-carbon content, highly hardenable, with high ability to forge (forgability). It is used extensively for driveshafts, gears and axles, bolts, studs, and in the automotive industry. The AISI 1078 steel is selected whenever high strength is required. It is typically used to manufacture springs, edge tools, wear-resistant components, and scraper blades. The AISI 4140 steel is a Cr-Mo, medium-carbon steel with high hardenability and good fatigue, impact, and abrasion resistance. It is used for gears and pinions, balls, studs, and high-strength forgings such as crankshafts. AISI 4340 is similar to 4140 in composition with the addition of about 2% Ni and slightly more molybdenum in order to increase its toughness and strength. It is used for forging dies, die blocks, gears, and machine parts.

## 2. Experimental Procedure

### 2.1 Materials

The workability experiments were carried out on five commercial grades of steels: AISI 1018, 1045, 1078, 4140, and 4340. The materials were received as hot-rolled rods with diameter of 25 mm. The materials were annealed by heating to 865 °C for 1 h and then cooling to room temperature in the furnace.

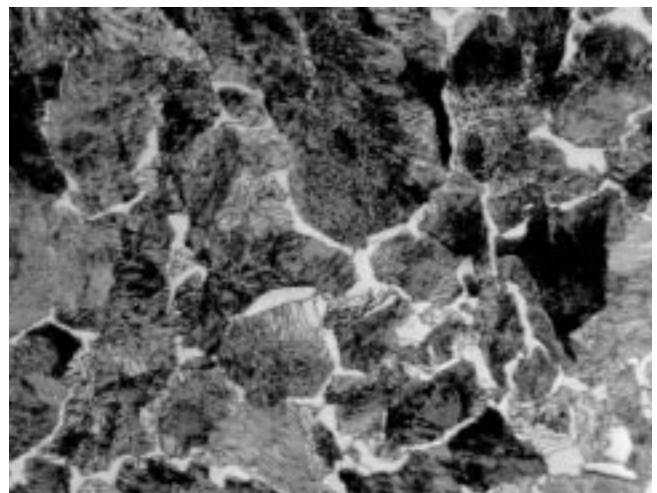
The chemical compositions of the five grades of steel are given in Table 1.

**Table 1** Chemical compositions of steels used in workability tests

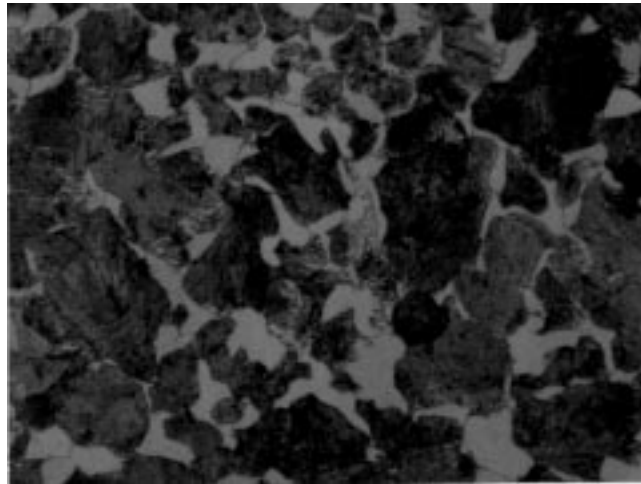
AISI No.	Composition, %								
	C	Mn	P	S	Si	Ni	Cr	Mo	Cu
1018	0.18	0.8	0.04	0.05	...	...	...	...	...
1045	0.45	0.8	0.05	0.05	...	0.06	...	...	...
1078	0.78	0.32	0.04	0.05	...	0.13	0.11	0.01	...
4140	0.4	0.8	0.017	0.02	0.18	...	1.05	0.20	...
4340A	0.4	0.8	0.023	0.02	0.28	1.85	0.8	0.26	0.12



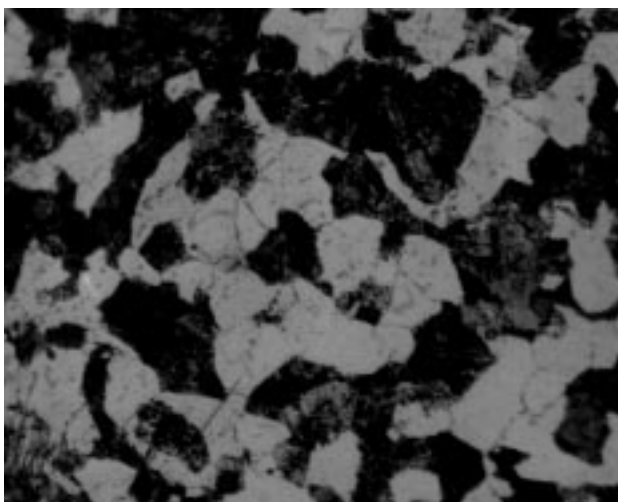
(a)



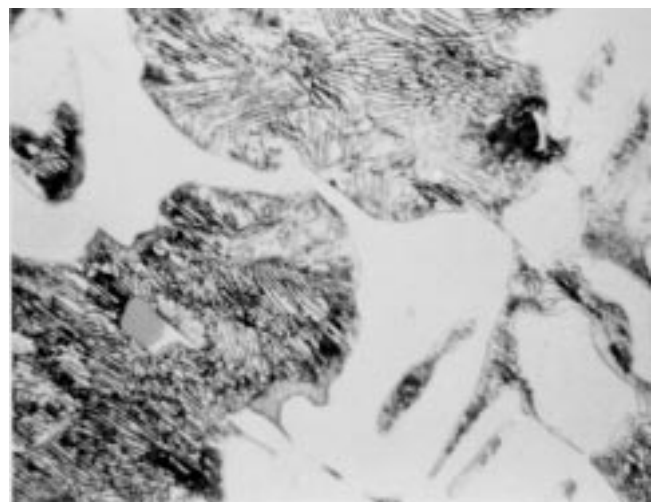
(b)



(c)



(d)



(e)

**Fig. 1** Microstructures of the steels used in the present study. (a) AISI 1018. 250 $\times$ . (b) AISI 1078. 500 $\times$ . (c) AISI 1045. 500 $\times$ . (d) AISI 4140. 500 $\times$ . (e) AISI 4340. 750 $\times$

The mechanical properties of the five grades of steel were determined according to ASTM E 8-82 specifications for tensile testing and also by compression testing according to the standard ASTM E 9-81. The diameter of the tensile test specimen was 12.5 mm, while the diameter of the compression specimen was 20 mm and  $H_0/D_0$  equaled 1. The friction during the compression test was minimized by applying a polytetrafluoroethylene (PTFE) spray on the specimens and die surfaces before testing. The microstructures of the materials used in the present work are shown in Fig. 1.

## 2.2 Workability Tests

The upset tests were performed on cylindrical, tapered, flanged, and ring specimens to obtain different strain paths. The specimens were machined out of supplied rods of 25 mm diameter according to the dimensions and geometries shown in Table 2.

A grid pattern was marked on the specimen surface. Measurements of the grid spacing for different elements on the specimen surface were conducted for several reductions in height ratio during compression testing. The elements exactly on the equator and the elements located at midheight between the

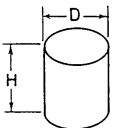
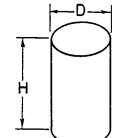
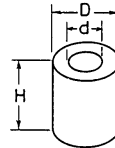
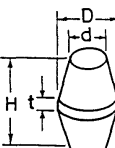
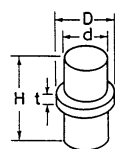
equator and the top surface of the specimens as well as elements close to the die/specimen interface were carefully observed for any crack initiation. The measurements of the grid spacing were carried out at several reductions in height of the specimens during testing by using a toolmaker's microscope equipped with an  $x$ - $y$  measurement micrometer table. The axial and the circumferential strains were calculated for each element from the measurements obtained according to:

$$\varepsilon_z = \ln \left( \frac{h_i}{h_o} \right) \quad \varepsilon_\theta = \ln \left( \frac{w_i}{w_o} \right)$$

where  $h_o$  and  $w_o$  are the initial height and width of an element, respectively, and  $h_i$  and  $w_i$  are the current height and width of the element, respectively. The upset tests were performed on a 50 MN Instron testing machine that was connected to a computer to record the load-displacement curves. The upset test was stopped when crack initiation site was observed.

From the measurements obtained, the strain path of each element was determined and drawn on the forming-limit diagram (FLD). The end of the strain path represents the point at

**Table 2 Geometries and dimensions of specimens for workability tests**

	Workability test	Height (H), mm	Diameter (D), mm	Diameter (d), mm	Thickness (t), mm
	Solid cylindrical $H/D = 1$	20	20	...	...
	Solid cylindrical $H/D = 1.5$	30	20	...	...
	Ring $H/D = 1$	20	20	10	...
	Tapered	30	20	10	5
	Flanged	30	26	20	5

which cracking starts to initiate. Connecting these ends of different strain paths, the workability limit or the fracture limit was obtained for each type of steel.

### 3. Experimental Results and Discussion

The flow curves for the five grades of steel under the present investigation were determined by tension and compression tests as mentioned in the previous section. The results obtained from the tension test are shown in Fig. 2. The same data were plotted using the logarithmic scales, as shown in Fig. 3, in order to determine the constant  $K$  (strength coefficient) and  $n$  (strain-hardening exponent) in the constitutive equation  $\bar{\sigma} = K\bar{\epsilon}^n$ . This power-law equation was considered to represent the flow equation of the material at room temperature. The values obtained

for  $K$  and  $n$  are shown in Table 3. The elongation as well as the reduction in area as a measure of ductility are also given in Table 3.

It is shown from the results in Table 3 and Fig. 2 that AISI 1078 steel has the lowest ductility, while AISI 4340 shows the highest flow curve as well as good ductility.

The flow curves obtained by the compression test of cylindrical specimens are shown in Fig. 4. The same results are also shown in Fig. 5 on a logarithmic scale.

The upset (compression) test was carried out on different specimens shown in Table 2 to determine the workability limits of the different grades of steel. During the tests, the load versus

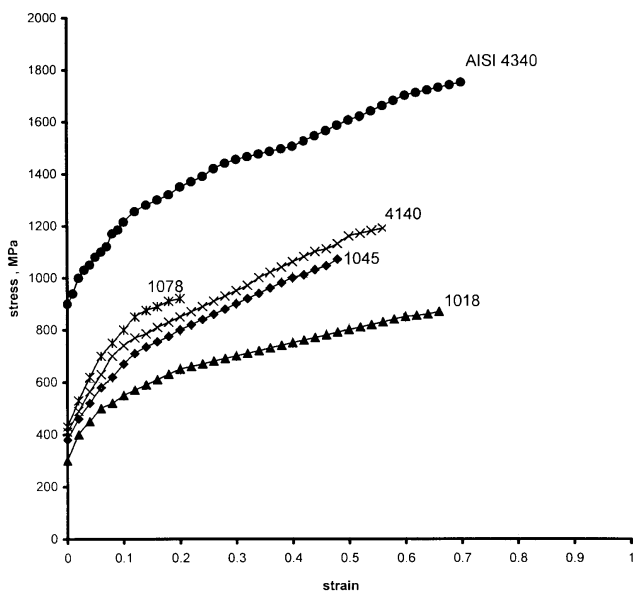


**Fig. 2** Tensile stress-strain curves for five grades of steel at room temperature

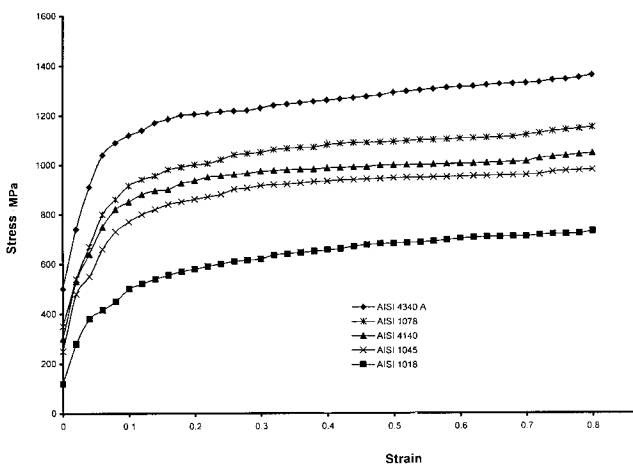


**Fig. 4** Stress-strain curves from compression tests at room temperature

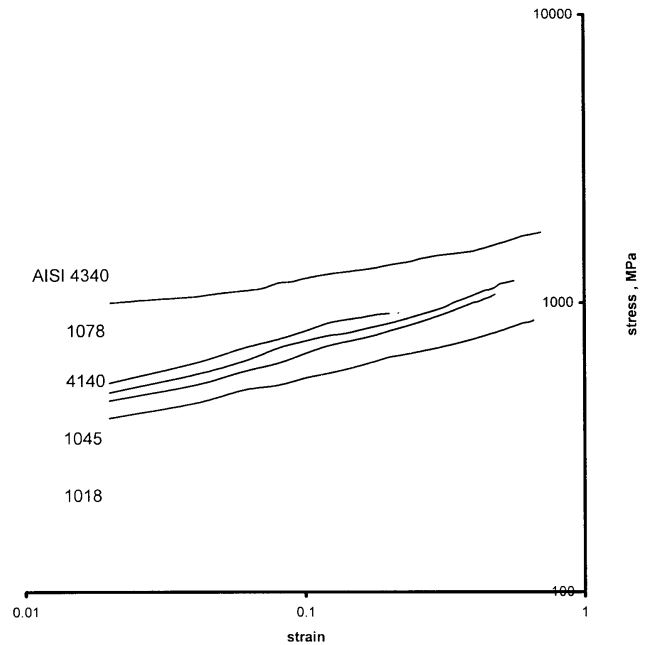


**Fig. 3** Logarithmic plot for tensile stress-strain curves

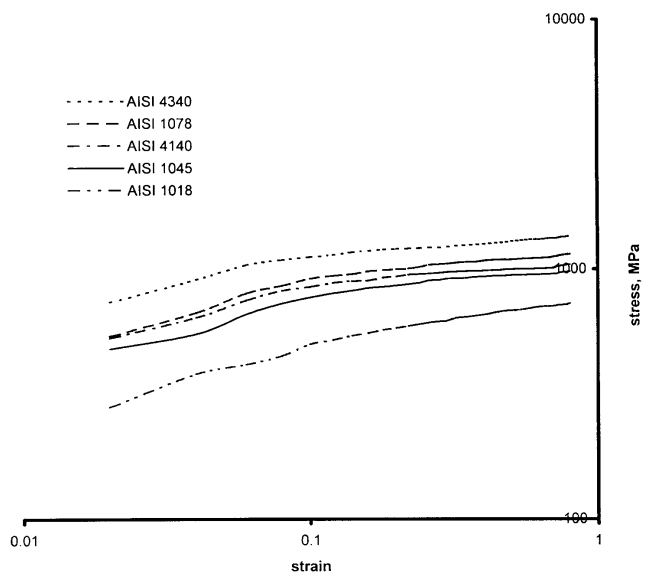


**Fig. 5** Logarithmic plot for stress-strain curves from compression tests

the axial displacement as well as the dimensions of the grid elements were measured. The data shown in Fig. 6 are an example of forming load versus the axial displacement obtained by testing cylindrical specimens machined out of the five grades of steel.

From the workability tests on AISI 1045 steel, the experimentally determined values for the axial and circumferential strains were plotted on the FLD shown in Fig. 7. Thirteen strain paths obtained from all types of specimens are given with different symbols as shown in Fig. 7. The strain paths obtained from cylindrical specimens with aspect ratios 1 and 1.5 deviated from the line with slope  $-0.5$ , which represents homogeneous deformation (frictionless compression). The deviation increased as barreling developed. Flanged specimens exhibited a strain path of slope approximately  $-2$ , which is similar to that found in axial tension. This is because very little axial compression was applied to the rim during the circumferential expansion caused by compressive deformation of the specimen. Tapered specimens gave strain paths with slopes ranging between  $-2$  and  $-0.5$ . It is worth noting that all strain paths obtained from different elements and different specimens exhibited nonlinearity from the beginning to the end of the strain path. Therefore, no one slope could be obtained from one

strain path, and the slope is not a unique value at all points along the strain path. It is also interesting to note that the slope at a point on the strain path increases as that point moves toward the end of the strain path or the fracture point. This means that at the fracture point, the incremental axial strain component ( $d\epsilon_z$ ) is almost zero, while the incremental hoop strain component ( $d\epsilon_\theta$ ) is very high. This change in the slope of the strain path has a great effect on the stress state at the surface of the specimen.

The scatter in the experimental data for axial and hoop strains along the strain path makes the determination of the slope of the strain path extremely difficult. Therefore, the curve-fitting technique was used to obtain a smooth relationship between the axial strain ( $\epsilon_z$ ) and the hoop strain ( $\epsilon_\theta$ ). This relationship represents the equations of the strain paths. Some of these equations for thirteen strain paths obtained from different specimens geometries for 1045 steel are given in Appendix A.

The ends of the strain paths represent the fracture points. Joining all the fracture points on all strain paths gave the workability limit for AISI 1045 steel as shown in Fig. 8. In this figure, the area under the workability limit is the safe area and no fracture will occur along any strain path in this area, while the area above the workability limit is the fracture area.

**Table 3 Mechanical and flow properties of the five grades of steel used in the present work**

AISI No.	Tensile strength, MPa	Yield strength, MPa	Elongation, %	Reduction in area, %	Strength coefficient (K), MPa	Strain-hardening exponent, $n$
1018	400	290	36.5	68	950	0.256
1045	518	353	30	57	1350	0.328
1078	615	375	24	25	1380	0.324
4140	655	417	26	57	1370	0.32
4340	745	428	32	50	1840	0.18

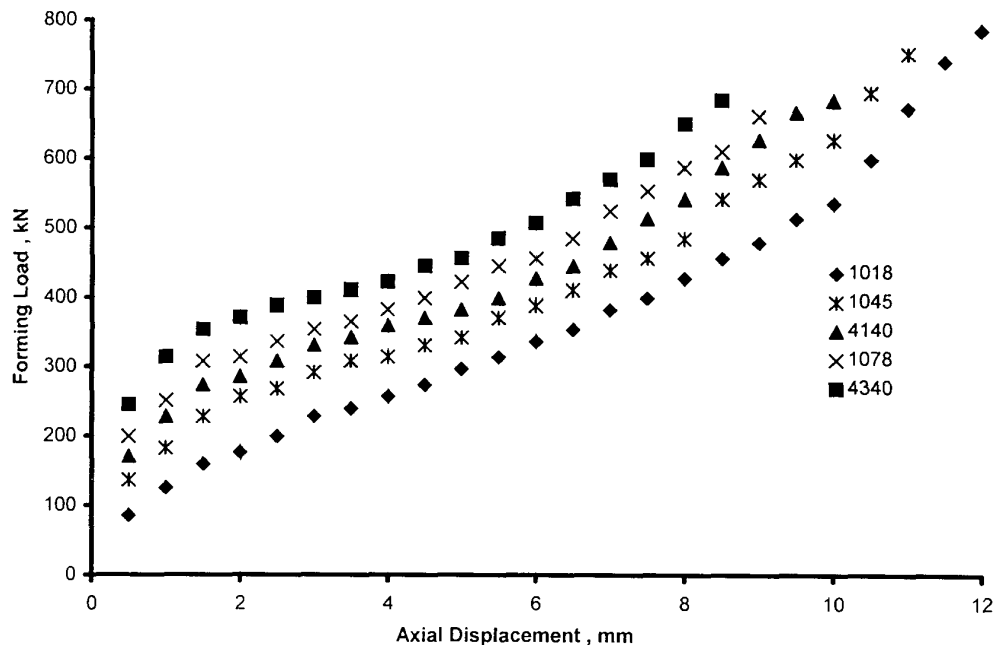


**Fig. 6** Forming load versus axial displacement obtained by upset test of cylindrical specimens

The effect of the slope of the strain path ( $\beta$ ) on the state of stress on the specimen surface can be determined from the plasticity equation and Von-Mises yield criteria as given in Appendix B.

Equations 1 to 3 from Appendix B are plotted to show the variation of the stress components as functions of  $\beta$ . The results are shown in Fig. 9.  $\beta$  is considered to vary in the range from  $-0.5$  up to  $-4$ . It is shown that the mean stress (hydrostatic component,  $\sigma_m/\bar{\sigma}$ ) becomes positive when  $\beta < -1$ . Ductile fracture usually starts when the mean stress or the hydrostatic stress component is positive.

The normalized mean stress component ( $\sigma_m/\bar{\sigma}$ ) is zero for  $\beta = -1$ , which is the case of pure shear deformation, while it is negative for homogeneous compression ( $\beta = -0.5$ ). Increasing the slope of the strain path to higher negative values such as  $\beta$

$= -2$  produces a condition similar to pure tension. The stress-formability index (FI), which is defined by  $(3\sigma_m/\bar{\sigma})$  in Ref 34, can also be evaluated for each strain path at the fracture point using Eq 1. The correlation between FI and both the equivalent strain ( $\bar{\epsilon}$ ) and the axial strain ( $\epsilon_z$ ) are obtained using Eq 1 and 4 from Appendix B, and the results are shown in Fig. 10. The maximum values for  $\bar{\epsilon}$  and  $\epsilon_z$  are obtained when the formability index equals 1.

The slope of the strain path has great effect on the state of stress on the free surface. The hoop (circumferential) tensile stress  $\sigma_\theta$  has a strong influence on workability because it acts normal to the longitudinal surface defects and the mechanical fibering (grain orientation) of the material. This will open up the defects and possibly produce longitudinal cracks. For fric-

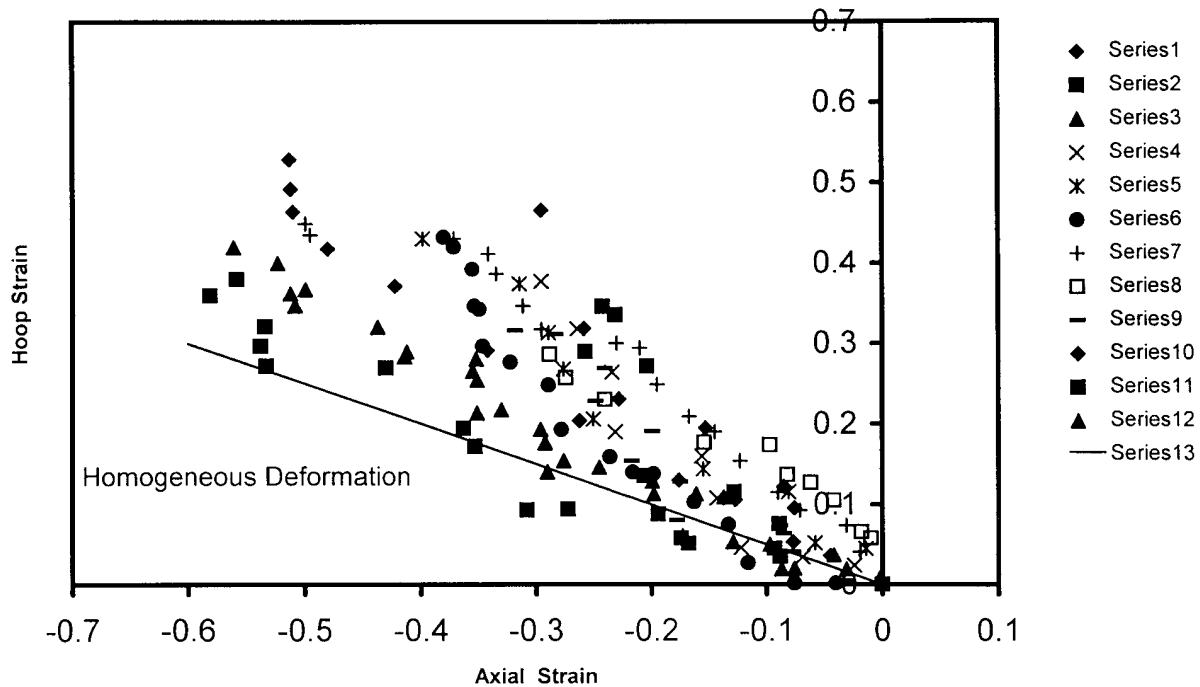


Fig. 7 Strain paths obtained by testing different specimen geometries machined out of AISI 1045 steel

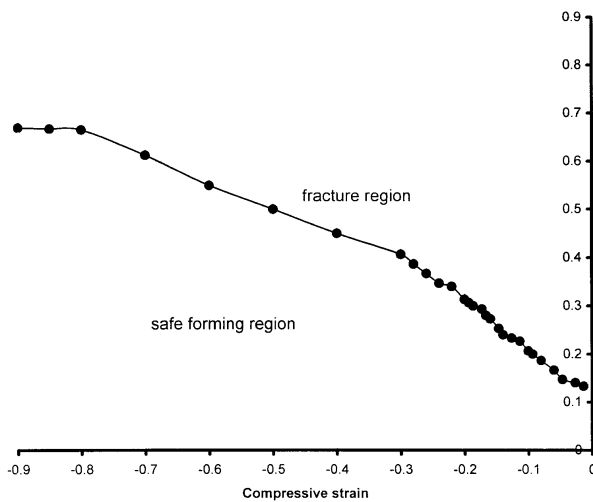


Fig. 8 Workability limit for AISI 1045 steel

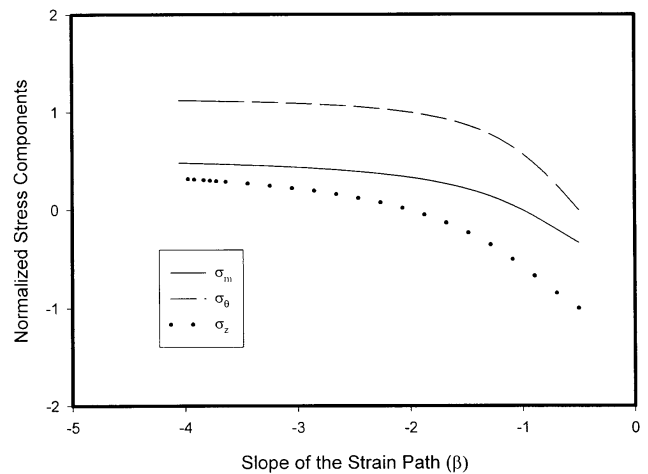
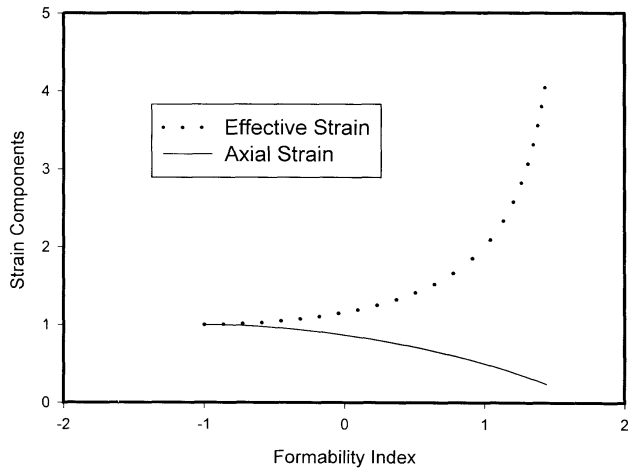


Fig. 9 Stress components as function of the slope of the strain path



tionless (homogeneous) deformation,  $\sigma_\theta$  is almost zero, and the longitudinal surface defect will not be a source of fracture. Under nonhomogeneous deformation (i.e., the slope of the strain path has higher negative values than  $-0.5$ ),  $\sigma_\theta$  becomes more positive and also the mean hydrostatic pressure ( $\sigma_m$ ) becomes less compressive, which leads to fracture. The axial stress  $\sigma_z$  and the mean stress  $\sigma_m$  increase rapidly during compression testing on the shorter specimens. For tests on longer specimens, these stresses increase more gradually. For both sizes,  $\sigma_m$  is tensile over a large part of the compression test and in the final stages is of the order of one-third the flow stress, as shown in Fig. 9.



**Fig. 10** Normalized strain components as function of the formability index

The experimental fracture locus for AISI 1045 steel obtained by joining the fracture points of all strain paths is shown in Fig. 8. This fracture locus can be approximated by three line segments. The first segment is almost parallel to the homogeneous deformation line ( $\beta = -0.5$ ). The second segment has less slope than the first segment and intersects the third segment, which has zero slope (i.e.,  $\epsilon_\theta = \text{constant}$ ). The fracture locus for all other types of steels are obtained, and the results are shown in Fig. 11. This figure represents the FLD. It is clearly shown that the AISI 1018 steel has the highest level for its FLD, while AISI 1078 has the lowest level when compared with all other types of steels.

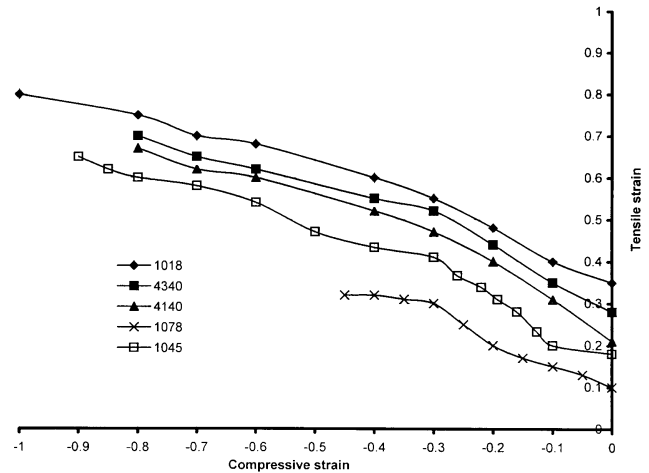


**Fig. 11** Workability limits for five grades of steel

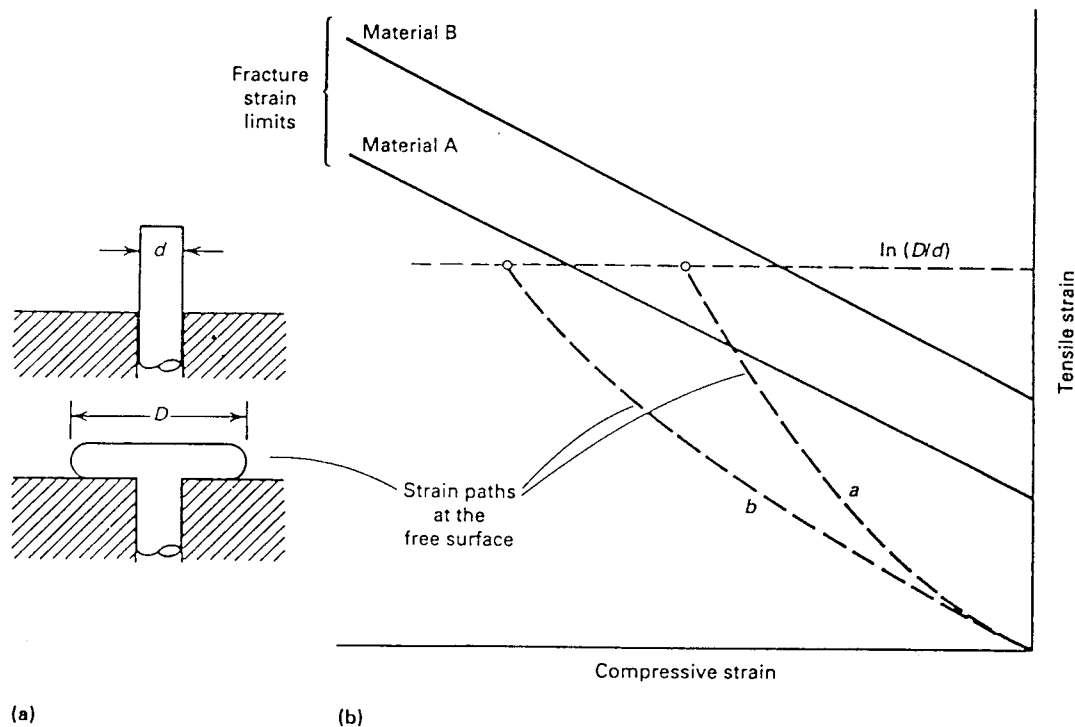
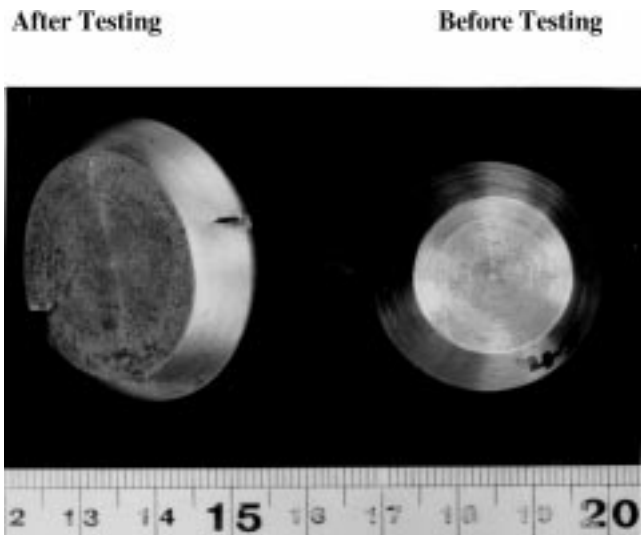
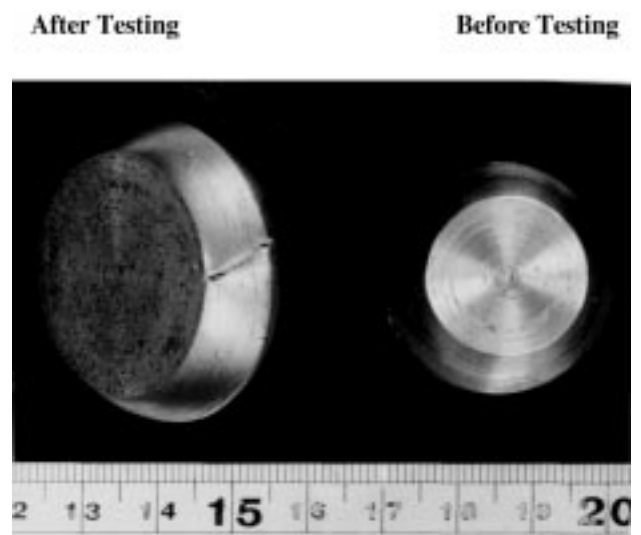


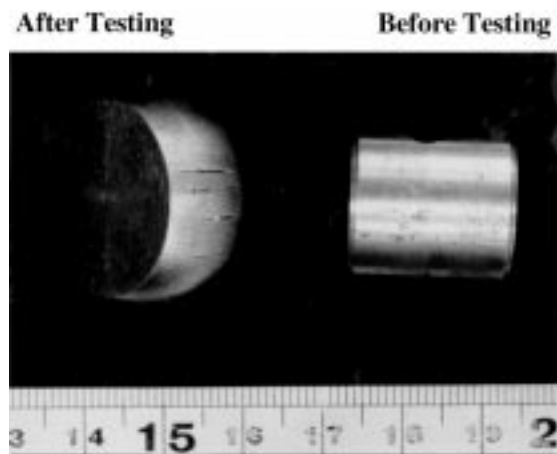
**Fig. 12** Application of the workability diagram in design and manufacture processes. Upsetting (a) of bar diameter  $d$  to head diameter  $D$ . (b) Material fracture strain limits are superimposed on strain paths reaching the final required strain. Strain path b (low friction) prevents fracture for both materials. Material B avoids fracture for either strain path.



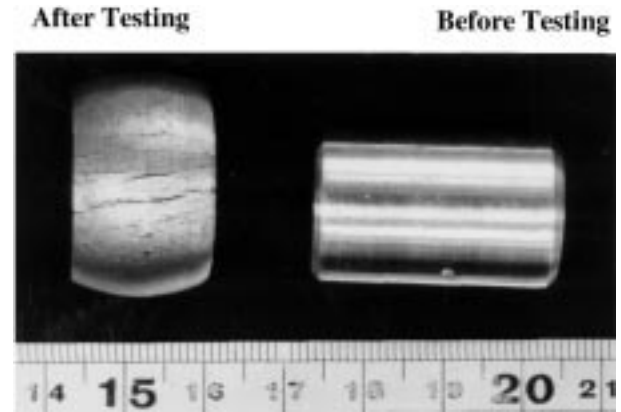
(a)



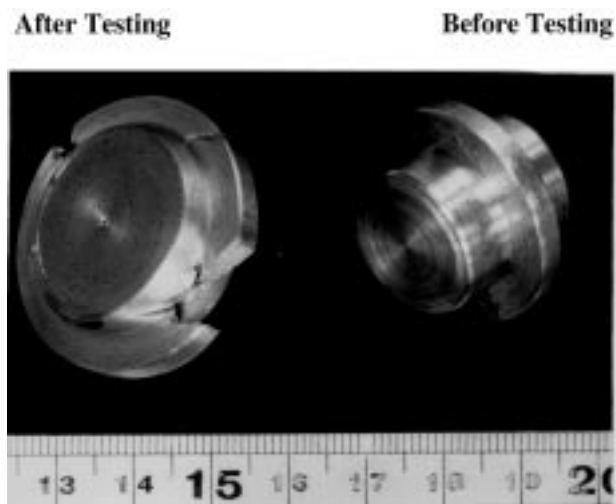
(b)



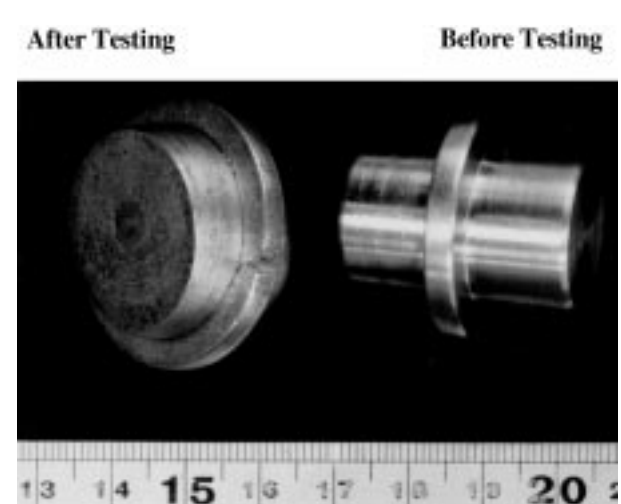
(c)



(d)



(e)



(f)

**Fig. 13** Modes of surface cracking for different specimen geometries. (a) Short taper specimen. (b) Long taper specimen. (c) Short cylindrical specimen. (d) Long cylindrical specimen. (e) Short flanged specimen. (f) Long flanged specimen

The FLD shown in Fig. 11 has practical application as a tool for troubleshooting fracture problems in an existing process or for design and modification of new products. Safe and unsafe forming conditions are usually determined with the aid of the FLD. The behavior of the deformed material under certain process parameters is determined by the configuration of the strain path for some critical elements in the workpiece. The strain path represents the  $\epsilon_\theta$  and the  $\epsilon_z$  components through the entire deformation process. The intersection of the strain path with the fracture locus (FLD) leads to fracture. To avoid fracture, it is possible to choose a material with higher level of FLD or to alter the strain path. The latter option represents a process change that involves improved lubrication condition and modifying the die design and workpiece (preform) design. The two options are represented schematically on an FLD as shown in Fig. 12, which is taken from Ref 2. Therefore, the results shown in Fig. 11 have practical importance in the design and manufacture of a product made from any one of the five grades of steel used in the present study.

Another use of the data in Fig. 11 is the determination of the constants of the empirical fracture criterion that are available in the literature (Ref 1, 2, and 29). Once the constants have been determined, the criterion can be used in a finite-element program to predict the fracture strain during the forming process as it has been carried out in Ref 30.

The longitudinal crack and the oblique crack were obtained as the two major modes of surface fractures. The mode of fracture depends mainly on the state of stress and the state of strain, both of which in turn depend on the degree of deformation and the slope of the strain path. The longitudinal crack is usually obtained when the axial surface stress is tensile, while the oblique crack is obtained when the axial surface stress is compressive. Figure 13 shows the two types of cracks on the surfaces of different specimens.

## 4. Conclusions

The present detailed studies on five different grades of steel provide a complete history of  $\epsilon_\theta$  and  $\epsilon_z$  by testing specimens with various geometries. Also, the workability limit for each type of steel has been determined experimentally. The workability limit is a useful tool in the design and manufacture phases of any product. It can also be used in examining or deriving criteria for ductile fracture during plastic deformation of any product with a predetermined strain path according to the geometry of the product and the forming dies.

The present study also shows that the relationship between the circumferential strain and axial strain increments ( $d\epsilon_\theta$ ,  $d\epsilon_z$ ) is continuously changing with increasing deformation. As a result, the slope of the strain path ( $\beta = d\epsilon_\theta/d\epsilon_z$ ) increases to high negative values at the end of the deformation. This high value of the slope is the main cause of developing  $\sigma_m$  and the high values for  $\sigma_\theta$  that cause ductile fracture.

## Acknowledgment

We would like to extend our deep appreciation and thanks to Ms. Amy Juliana Noronha for typing the original manuscript.

## References

1. G.E. Dieter, Workability Tests, *Forming and Forging*, Vol 14, *Metals Handbook*, 9th ed., S.L. Semiatin, Ed., ASM International, 1988, p 363-387
2. H.A. Kuhn, Workability Theory and Application in Bulk Forming Processes, *Forming and Forging*, Vol 14, *Metals Handbook*, 9th ed., S.L. Semiatin, Ed., ASM International, 1988, p 388-404
3. H. Kudo and K. Aoi, Effect of Compression Test Conditions upon Fracturing of a Medium Carbon Steel—Study on Cold Forgability Test: Part II, *J. Jpn. Soc. Technol. Plast.*, Vol 8, 1967, p 17-72 (in Japanese)
4. H. Kudo, K. Sato, and K. Aoi, On Cold Forgability Test, *CIRP Ann.*, Vol XVI, 1968, p 309-318
5. S. Kobayashi, Deformation Characteristics of Ductile Fracture of 1040 Steel in Simple Upsetting of Solid Cylinders and Rings, *J. Eng. Ind. (Trans. ASME)*, May 1970, p 391-399
6. A.L. Hoffmann, The Use of Workability Test Results to Predict Processing Limits, *Proc. Symp. Relation between Theory and Practice of Metal Forming* (Cleveland, OH), Oct 1970, Plenum Press, 1971, p 349-391
7. D.C. Shah, Use of Metallic Materials to Model the Flow and Fracture of Steel in Cold Upsetting, *Mechanical Working and Steel Processing XIV* (Dalton, IL), 23-24 Jan 1974, A. Marcan-tonio, Ed., AIME, p 285-300
8. B.S. Levy and T.E. Fine, Effect of Composition and Process Variables on Deformation in Simple Upsetting, *Mechanical Working and Steel Processing Conf. VI*, AIME, 1973, p 105-126
9. P.F. Thomason, Tensile Plastic Instability and Ductile Fracture Criteria in Uniaxial Compression Tests, *Int. J. Mech. Sci.*, Vol 11, 1969, p 187-198
10. P.F. Thomason, The Use of Pure Aluminum as an Analogue for the History of Plastic Flow, in Studies of Ductile Fracture Criteria in Steel Compression Specimens, *Int. J. Mech. Sci.*, Vol 10, 1968, p 501-518
11. H.A. Kuhn and P.W. Lee, Strain Instability and Fracture at the Surface of Upset Cylinders, *Metall. Trans.*, Vol 2, Nov 1971, p 3197-3202
12. P.W. Lee and H.A. Kuhn, Fracture in Cold Upset Forging—A Criterion and Model, *Metall. Trans.*, Vol 4, 1972, p 969-974
13. S.M. Woodall and J.A. Schey, Determination of Ductility for Bulk Deformation, *Formability Topics—Metallic Materials*, STP 647, American Society for Testing and Materials, 1978, p 191-205
14. S.I. Oh and S. Kobayashi, Workability of Aluminum Alloy 7075-T6 in Upsetting and Rolling, *J. Eng. Ind. (Trans. ASME)*, Aug 1976, p 800-806
15. P. Bariani, Cold Workability Limits of 1100 Aluminum, 2024 and 7075 Aluminum Alloys in Isothermal and Adiabatic Upsetting Tests, *Adv. Technol. Plast.*, Vol 11, 1984, p 857-865
16. J. Shah and H.A. Kuhn, An Empirical Formula for Workability Limits in Cold Upsetting and Bolt Heading, *J. Appl. Metalwork.*, Vol 4 (No. 3), July 1986, p 255-261
17. E. Erman, H.A. Kuhn, and G. Fitzsimons, *Novel Test Specimens for Workability Testing*, STP 808, ASTM, 1983, p 279-290
18. S. Kiviruori and M. Sulonen, Formability Limits and Fracturing Modes of Uniaxial Compression Specimens, *CIRP Ann.*, Vol 27 (No. 1), Jan 1978, p 141-145
19. G. Sornberger, F. Ramparany, J.M. Cerles, and D. Teirlinck, Ductility of a Continuous Cast 5056 Aluminum Alloy Rod, *Formability and Metallurgical Structure*, Proc. Symp., Mechanical Metallurgy and Shaping and Forming Committees of TMS, AIME (Orlando, FL), 5-9 Oct 1986, p 327-340
20. P.F. Thomason, The Free Surface Ductility of Uniaxial Compression Specimens with Longitudinal Surface Defects, *Int. J. Mech. Sci.*, Vol 11, 1969, p 65-73

21. M. Mayagawa, M. Shinohara, H. and Asao, Compression Test of Cylinders with Longitudinal Notches for Comparison of Cold Upset—Forgeability, *J. Jpn. Soc. Technol. Plast.*, Vol 12 (No. 122), 1971, p 183
22. T. Fukuda and H. Hajita, Effect of Longitudinal Surface Defect on the Steel Wire on Upsetting Limits, *J. Jpn. Soc. Technol. Plast.*, Vol 16 (No. 170), 1975, p 255-263
23. M. Kojima and Y. Tozawa, Effect of Upsetting Condition and Specimen Groove on Upset Limit, Study on Upsetting of Pre-deformed Material II, *J. Jpn. Soc. Technol. Plast.*, Vol 12 (No. 131), 1971, p 903-909
24. Z. Fan, The Grain Size Dependence of Ductile Fracture Toughness of Polycrystalline Metals and Alloys, *Mater. Sci. Eng.*, Vol A191, 1995, p 73-83
25. A. El-Domiati and M. Shaker, A Note on the Workability of Porous-Steel Preforms, *J. Mater. Process. Technol.*, Vol 25, 1991, p 229-233
26. S.E. Clift, P. Hartley, C.E.N. Sturgess, and G.W. Rowe, Fracture Prediction in Plastic Deformation Processes, *Int. J. Mech. Sci.*, Vol 32 (No. 1), 1990, p 1-17
27. Y.Y. Zhu, S. Cescotto, and A.M. Habraken, A Fully Coupled Elastic-Plastic Damage Modeling and Fracture Criteria in Metal Forming Processes, *J. Mater. Process. Technol.*, Vol 32, 1992, p 197-206
28. A.S. Wifi, A.H. El-Monayri, and N. El-Abassi, Finite Element Determination of Workability Limits for Disks and Rings under Different Upsetting Conditions, *Adv. Mater. Process. Technol.*, Vol 33, 1992, p 1731-1739
29. M.A. Shabara, A.A. El-Domiati, and A. Kandil, Validity Assessment of Ductile Fracture Criteria in Cold Forming, *J. Mater. Eng. Perform.*, Vol 5 (No. 4), Aug 1996, p 478-488
30. B.P.P.A. Gouveia, J.M.C. Rodrigues, and P.A.F. Martins, Fracture Predicting in Bulk Metal Forming, *Int. J. Mech. Sci.*, Vol 38 (No. 4), 1996, p 361-372
31. V. Vujovic and A.H. Shabaik, A New Workability Criterion for Ductile Metals, *J. Eng. Mater. Technol. (Trans. ASME)*, Vol 108, 1986, p 245-249
32. H.W. Wagener and J. Hatts, Cold Extrusion and Machinability of Free-Machining Steels, *J. Mater. Process. Technol.*, Vol 24, 1990, p 235-244
33. H.W. Wagener and J. Wolf, Cold Forming of MMC's of Al Alloy Matrix, *J. Mater. Process. Technol.*, Vol 37, 1993, p 253-265
34. M. Abdel-Rahman, Determination of Workability Curve Using Two Mechanical Tests, *J. Mater. Process. Technol.*, Vol 51, 1995, p 50-63

---



---

## Appendix A: Experimental Strain Path Equations

Equations obtained by the best-fit technique for the experimental strain components of different strain paths when AISI 1045 steel specimens were tested by compression (Fig. 7).

Strain path No.	Equation
1	$\epsilon_{\theta} = -0.976 \epsilon_z + 1.235 \epsilon_z^2 + 1.72 \epsilon_z^3$
2	$\epsilon_{\theta} = -0.5 \epsilon_z + 2.7 \epsilon_z^2 + 3.4 \epsilon_z^3$
3	$\epsilon_{\theta} = -0.92 \epsilon_z + 0.5 \epsilon_z^2 + 1.2 \epsilon_z^3$
4	$\epsilon_{\theta} = -0.93 \epsilon_z + 2.7 \epsilon_z^2 + 2.3 \epsilon_z^3$
5	$\epsilon_{\theta} = -0.23 \epsilon_z + 0.67 \epsilon_z^2 + 1.6 \epsilon_z^3$
6	$\epsilon_{\theta} = -0.763 \epsilon_z + 0.78 \epsilon_z^2 + 2.5 \epsilon_z^3$
7	$\epsilon_{\theta} = -2.7 \epsilon_z + 0.01 \epsilon_z^2 + 1.25 \epsilon_z^3$
8	$\epsilon_{\theta} = -0.56 \epsilon_z + 1.85 \epsilon_z^2 + 1.2 \epsilon_z^3$
9	$\epsilon_{\theta} = -0.635 \epsilon_z + 0.897 \epsilon_z^2 + 1.5 \epsilon_z^3$
10	$\epsilon_{\theta} = -0.5 \epsilon_z + 0.62 \epsilon_z^2 + 2.1 \epsilon_z^3$
11	$\epsilon_{\theta} = -1.1 \epsilon_z + 1.8 \epsilon_z^2 + 1.87 \epsilon_z^3$
12	$\epsilon_{\theta} = -1.2 \epsilon_z + 2.7 \epsilon_z^2 + 2.35 \epsilon_z^3$
13	$\epsilon_{\theta} = -2.1 \epsilon_z + 3.1 \epsilon_z^2 + 3.8 \epsilon_z^3$

# Appendix B: Stress Components as a Function of the Slope of the Strain Path ( $\beta$ )

The plastic-strain increment at any instant during the deformation process is proportional to the stress deviatoric tensor according to the Levy-Von Mises stress-strain relationships. For cylindrical coordinate system, the principal strain increments are given by:

$$d\varepsilon_r = \frac{d\bar{\varepsilon}}{\sigma} [\sigma_r - 0.5(\sigma_\theta + \sigma_z)]$$

$$d\varepsilon_\theta = \frac{d\bar{\varepsilon}}{\sigma} [\sigma_\theta - 0.5(\sigma_r + \sigma_z)]$$

$$d\varepsilon_z = \frac{d\bar{\varepsilon}}{\sigma} [\sigma_z - 0.5(\sigma_r + \sigma_\theta)]$$

During compression testing, the stress in the radial direction  $\sigma_r$  at the specimen surface is zero. Considering the slope of the strain path  $\beta = d\varepsilon_\theta/d\varepsilon_z$ , the stress components acting on an element at the specimen surface are given by:

$$\frac{\sigma_\theta}{\sigma} = \frac{1}{\sqrt{3}} \frac{(2\beta + 1)}{\sqrt{\beta^2 + \beta + 1}} \quad (\text{Eq 1})$$

$$\frac{\sigma_z}{\sigma} = -\frac{1}{\sqrt{3}} \frac{(\beta + 2)}{\sqrt{\beta^2 + \beta + 1}} \quad (\text{Eq 2})$$

$$\frac{\sigma_m}{\sigma} = -\frac{1}{\sqrt{3}} \frac{(\beta + 1)}{\sqrt{\beta^2 + \beta + 1}} \quad (\text{Eq 3})$$

Also, the ratio between the hoop stress  $\sigma_\theta$  and the axial stress  $\sigma_z$  is given by:

$$\alpha = \frac{\sigma_\theta}{\sigma_z} = \frac{(2\beta + 1)}{(\beta + 2)}$$

The effective strain can also be determined along the strain path as:

$$\bar{\varepsilon} = \frac{2}{\sqrt{3}} \int_0^{\varepsilon_z} \sqrt{\beta^2 + \beta + 1} d\varepsilon_z$$

where

$$d\varepsilon_z = \frac{h_{i-1} - h_i}{h_i} = \frac{\Delta h_i}{h_i}$$

Then,  $\varepsilon_z = \int d\varepsilon_z$

$$\varepsilon_{z_i} = \varepsilon_{z_{i-1}} + d\varepsilon_z \quad (\text{Eq 4})$$

The axial strain increment ( $d\varepsilon_z$ ) was determined by current measurements of the change in height and the current height for an element on the surface of the specimen. The total axial strain ( $\varepsilon_z$ ) was obtained by numerical summation of the incremental values of  $d\varepsilon_z$  along the strain path by using Eq 4.